

Optimization of Charge Carrier Extraction in Colloidal Quantum Dots Short-Wave Infrared Photodiodes through Optical Engineering

Epimitheas Georgitzikis,* Pawel E. Malinowski, Jorick Maes, Afshin Hadipour, Zeger Hens, Paul Heremans, and David Cheyns

Colloidal quantum dots (QDs) have attracted scientific interest for infrared (IR) optoelectronic devices due to their bandgap tunability and the ease of fabrication on arbitrary substrates. In this work, short-wave IR photodetectors based on lead sulfide (PbS) QDs with high detectivity and low dark current is demonstrated. Using a combination of time-resolved photoluminescence, carrier transport, and capacitance–voltage measurements, it is proved that the charge carrier diffusion length in the QD layer is negligible such that only photogenerated charges in the space charge region can be collected. To maximize the carrier extraction, an optical model for PbS QD-based photodiodes is developed, and through optical engineering, the cavity at the wavelength of choice is optimized. This universal optimization recipe is applied to detectors sensitive to wavelengths above 1.4 μm , leading to external quantum efficiency of 30% and specific detectivity (D^*) in the range of 10^{12} Jones.

1. Introduction

Imaging in the infrared (IR) wavelength range is essential for many applications such as low-light/night vision, surveillance, sorting, biometrics, and medical diagnostics.^[1] As silicon cannot be used to detect wavelengths above 1000 nm, imagers designed for the short-wave infrared (SWIR) range are based on

semiconductors with a smaller bandgap such as InGaAs and HgCdTe, combined with a Si-based CMOS readout circuit in a so-called hybrid imager.^[2] These materials have been thoroughly investigated over the last years, leading to high performance detectors. However, such hybrid solution sets a fundamental limitation to the smallest pixel size that can be achieved and this leads to very expensive detectors. In that respect, colloidal quantum dots (QDs) are a very interesting material group for the fabrication of IR imagers due to their unique opto-electronic properties. Quantum confinement allows the tuning of the nanocrystal bandgap according to their size, enabling detection at different wavelengths of the IR spectrum, while their electrical properties depend on the proper selection of ligands.^[3] Additionally,

the fact that they can be dispersed in solution and deposited over a large area makes them great candidates for low cost sensors, since they can be facily integrated on top of the readout circuit enabling monolithic IR imagers.^[4–6]

A lot of scientific effort has been devoted in the last years on improving the performance of QD photodiodes by the use of more efficient ligand passivation techniques^[7–9] or the device stack optimization^[10,11] leading to very high external quantum efficiencies (EQE) in a broad wavelength spectrum (up to 1 μm). However, for imaging applications, additional figures of merit such as the signal-to-noise ratio, the detector response speed, and the detectivity in a specific and narrow wavelength range must be maximized. Recent studies demonstrated that larger diameter QDs are characterized by lower absorption coefficients making it harder to achieve high EQE values further in the IR region.^[12,13] In the state of the art, two types of PbS-based detectors are dominant for the SWIR wavelength region, namely photoconductors^[14,15] and photodiodes.^[16–18] Photoconductors rely on amplification gain and suffer from low response speed, which makes them inappropriate for megahertz imaging. Schottky diodes have led to high QE and fast SWIR detectors, but the high dark current is a limiting factor towards the realization of an actual imager. Photodiodes using n-p junctions have been studied and applied in solar cells^[19] and photodetectors.^[20] These devices can combine a low dark current and fast response.

E. Georgitzikis, Dr. P. E. Malinowski, Dr. A. Hadipour,
Prof. P. Heremans, Dr. D. Cheyns
IMEC VZW


Kapeldreef 75, 3001 Heverlee, Belgium
E-mail: Epimitheas.Georgitzikis@imec.be

E. Georgitzikis, Prof. P. Heremans
KU Leuven

Kasteelpark Arenberg 10, 3001 Heverlee, Belgium

J. Maes, Prof. Z. Hens
Physics and Chemistry of Nanostructures
Ghent University
Krijgslaan 281-S3, 9000 Ghent, Belgium

J. Maes, Prof. Z. Hens
Center for Nano- and Biophotonics (NB-Photonics)
Ghent University
9000 Ghent, Belgium

 The ORCID identification number(s) for the author(s) of this article can be found under <https://doi.org/10.1002/adfm.201804502>.

DOI: 10.1002/adfm.201804502

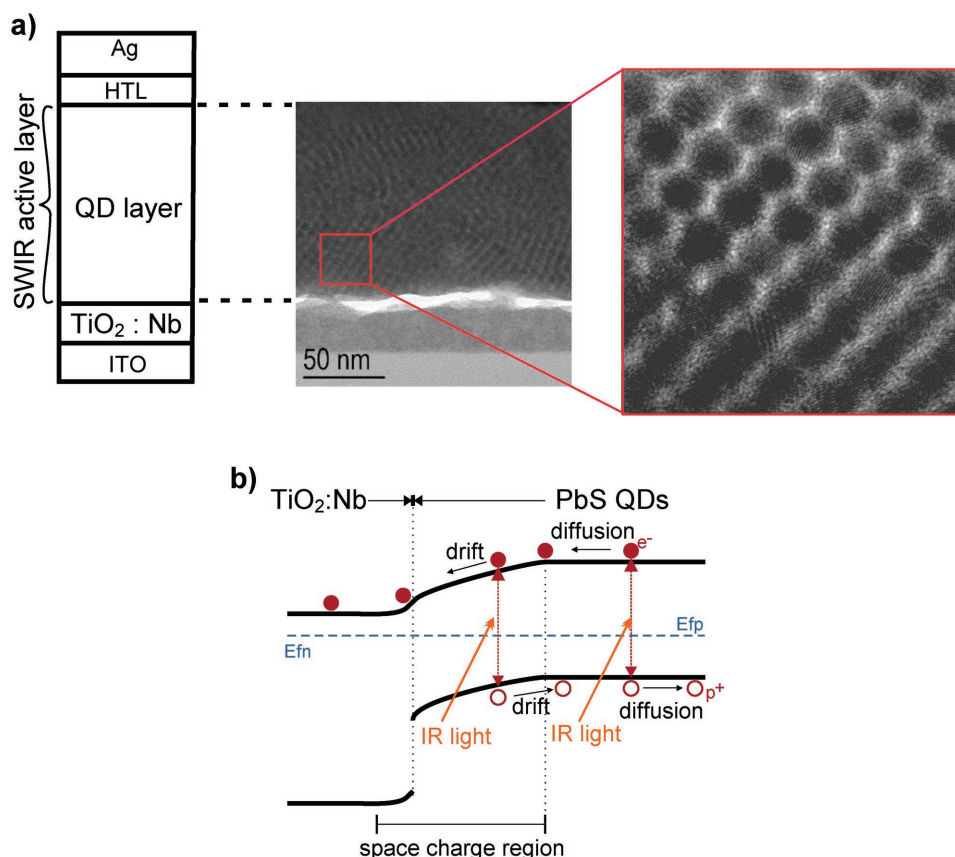


Figure 1. a) Photodiode stack architecture. The infrared photo-active layer is formed by a layer of PbS QDs. TEM shows the superlattice formed by the QDs and reveals high level of crystallinity. b) Schematic band diagram at equilibrium showing the p-n junction formed between the doped TiO₂ and the PbS QD layer and the drift and diffusion mechanisms.

In this work, we analyze the limits of the charge carrier extraction in colloidal QD photodetectors, and we apply this understanding in conjunction with optimization of the optical performance to maximize the efficiency of photodetectors at the wavelength of 1.4 microns. The charge carrier extraction mechanisms of narrow bandgap QD films are analyzed by time-resolved photoluminescence (TRPL), carrier transport, and capacitance–voltage measurements, enabling the determination of the carrier density, lifetime, and mobility. From the calculated short diffusion length of the minority carriers, we deduce the need to achieve a wide depletion region to minimize recombination and thus enhance the carrier harvesting. Subsequently, these data are used as feedback into process optimization of photodiodes based on an n-p heterojunction architecture, in which the junction is formed by a QD photoactive film and a metal oxide that acts as an n-type electron transport layer (ETL). Using optical modeling based on a transfer matrix method, we optimize the thickness of the transport layers to maximize the intrinsic cavity effect of the device structure at the wavelength that matches the IR absorption peak of the QDs, taking the limited depletion width into account. The result is a considerable boost in the QD layer absorption leading to high quantum efficiencies in the SWIR. In the fabricated devices, this boost is combined with a low dark current ($\approx \mu\text{A cm}^{-2}$), leading to specific detectivity in the range of 10^{12} Jones.

2. Results and Discussions

We selected PbS QDs with a diameter of 5.5 nm (see Experimental Section and Figure S1, Supporting Information) synthesized by hot-injection method.^[21] Here, the use of substituted thioureas enables the production of gram scale batches in a reproducible way. The NIR photoactive layer with a peak wavelength absorption at 1440 nm, is sandwiched between two transparent transport layers with good conductivity, and hence tunable thickness (see **Figure 1a** for the layer stack structure). The photodiode junction is created at the interface between the niobium-doped titanium dioxide layer (TiO₂:Nb)^[22] and the PbS QDs capped with 1,4-Benzenedithiol (1,4 BDT).^[23,24] Transmission electron microscope (TEM) inspection of the layer-by-layer grown QD layer revealed perfect crystallinity within the QDs, high level of super-crystallinity within a single layer, and random orientation between layers. Figure 1b depicts a schematic band diagram of the junction formed between the wide bandgap TiO₂:Nb and the PbS QDs, using energy level values from literature.^[25–29] The carriers that are photogenerated inside the space charge region will drift by the built-in potential to the respective electrode, while carriers that are generated in the quasi-neutral region must diffuse towards the space charge region in order to be collected. In the next sections, we present an in-depth analysis of the drift and diffusion mechanisms

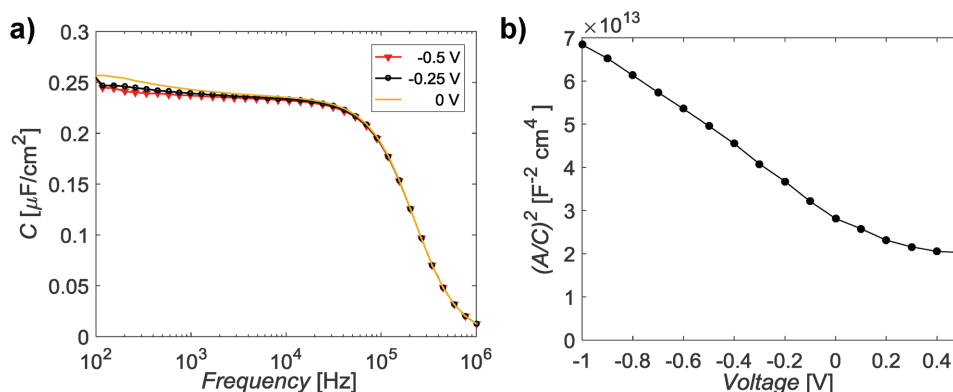


Figure 2. Capacitance–voltage measurements for Schottky diodes using a structure of ITO/QD/Al. a) Capacitance as a function of frequency at three bias conditions for a relatively thin PbS QD layer (≈ 50 nm). b) Mott–Schottky plot for a thick, not fully depleted PbS QD layer.

describing the transport of the photogenerated carriers and we quantitatively assess their limitations.

The electrical field in the space charge region of the photodiode causes carriers to drift towards the contacts. For a p-n junction, this space charge region originates from the carrier depletion from one side of the junction towards the layer with an opposite majority carrier profile. Assuming that the carrier concentration of the $\text{TiO}_2\text{:Nb}$ is much higher than the one of the QDs, we can consider a one-sided junction.^[26,27] The depletion width (W) of such a one-sided junction is

$$W = \sqrt{\frac{2 \epsilon_r \epsilon_0 (V_{\text{bi}} - V)}{q N_{\text{QD}}}} \quad (1)$$

where ϵ_r is the effective-medium dielectric constant of the QD layer, ϵ_0 is the vacuum permittivity, V_{bi} is the built-in potential, q is the elementary charge, and N_{QD} is the doping concentration of the QD film.^[30] In order to obtain ϵ_r and N_{QD} , capacitance–voltage (C–V) measurements are performed on Schottky diodes with a structure of ITO/PbS/Al. Assuming fully depleted devices (QD thickness 50–75 nm) are used to obtain the dielectric constant from the parallel plate capacitor model $C = (A\epsilon_r\epsilon_0)/d$, where A is the diode surface area and d is the PbS layer thickness. As shown in **Figure 2a**, the measured capacitance remains constant in the range of 10^2 – 10^5 Hz and for biases between -0.5 and 0 V, confirming that the diode is fully depleted. The dielectric constant can be accurately obtained at 14 ± 1 , a value that matches the results presented in literature through theoretical models.^[31]

To determine the doping concentration of the PbS QD absorber, a Schottky diode with the same structure as previously is processed, however this time a thick (≈ 250 nm) and thus not fully depleted PbS QD layer is used. Using the Mott–Schottky equation^[11]

$$\frac{1}{C^2} = \frac{2(V_{\text{bi}} - V)}{q \epsilon_r \epsilon_0 N_{\text{QD}}} \quad (2)$$

the N_{QD} is obtained from the slope of $1/C^2$ versus the applied bias and found to be in the range of 2.3×10^{17} and 3.1×10^{17} (Figure 2b). Then the carrier density and the determined dielectric constant are applied in Equation (1), in order to calculate

the depletion width in the p-n junction devices, which is found to be around 65 ± 10 nm at 0 V bias, while at 2 V reverse bias, it increases to 135 ± 10 nm. These values are also confirmed by performing C–V measurements on the p-n junction photodiodes and the voltage-dependent depletion width can be determined directly from $W = \epsilon_r\epsilon_0/C(V)$ (Figure S2, Supporting Information).

Charges photogenerated outside of the space charge region are required to diffuse across the quasi-neutral region to be collected by the respective electrode. The distance that the carriers can travel before they recombine is defined by their diffusion length, which can be calculated as

$$L = \sqrt{D \tau} \quad (3)$$

where τ is the carrier lifetime and D is the diffusion coefficient, linked to the charge carrier mobility μ via the Einstein–Smoluchowski relation $D = \frac{kT}{q} \mu$ (with k the Boltzmann’s constant, and T the temperature).

The carrier lifetime in the QD film is obtained using TRPL on glass/PbS layers. The PL decay as a function of time,^[32] (Figure 3a), corresponds to the decay of the minority carriers. From these data, we retrieve a minority carrier lifetime of only 15 ns.

To determine the carrier mobility in the PbS film, single carrier devices exhibiting space charge limited current (SCLC) are fabricated using an ITO/QD/Ag structure for electron-only devices and ITO/PEDOT:PSS/QD/MoO_x/Au for hole-only devices. Figure 3b shows a current density–voltage curve (J – V) and the results of the fitting obtained using the SCLC mechanism in a hole-only device. The results for an electron-only device are shown in Figure S3 in the Supporting Information. At low bias voltages (<0.1 V), the device follows an Ohmic behavior with J being proportional to V . As the bias increases, the injected carriers start to dominate, filling trap states of the film, and the current density becomes proportional to the square of the applied voltage ($J \sim V^2$). When all of the traps are filled, there is an exponential current increase, followed by another region with a $J \sim V^2$ behavior following the Mott–Gurney law,^[33]

$$J_{\text{MG}} = \frac{9}{8} \epsilon_r \epsilon_0 \mu \frac{V^2}{d^3} \quad (4)$$

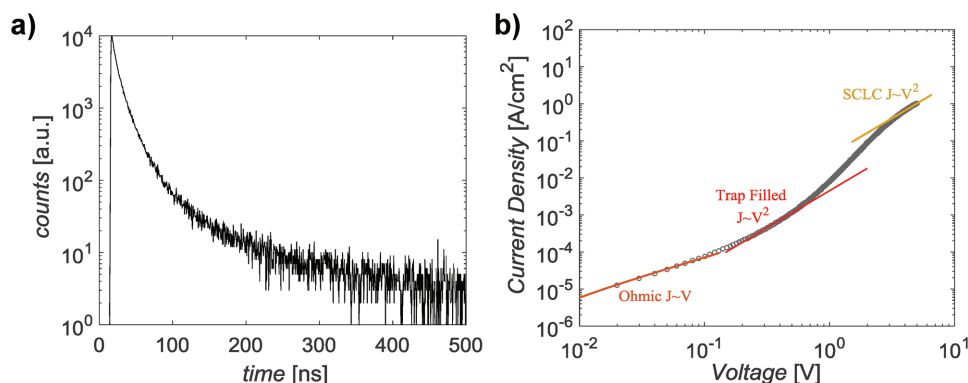


Figure 3. a) TRPL measurements lifetime spectra of 5.5 nm QDs capped with 1,4-BDT. b) J - V plot of single carrier PbS QD photodiode demonstrating the Ohmic, trap filled, and SCLC regions.

where d is the active layer thickness. From the Mott–Gurney region of the J - V curves, we extracted the mobility of holes and electrons in the range of $4 \times 10^{-5} \text{ cm}^2 \text{ V}^{-1} \text{ s}^{-1}$ and $1 \times 10^{-5} \text{ cm}^2 \text{ V}^{-1} \text{ s}^{-1}$, respectively.

Knowing the lifetime and mobility, the diffusion length of the minority carriers can be readily calculated from Equation (3) and is found to be extremely short – less than 1 nm. This result indicates that there is a limitation on the distance that the carriers can travel before they recombine; thus carrier extraction based on diffusion can be excluded. We conclude that for maximum photocurrent, we cannot rely on carrier diffusion, but rather, fully depleted devices should be considered.

Taking into consideration the preceding analysis, we determine that the maximum usable QD layer thickness in our photodiode structure falls in the range of the depletion width (maximum 150 nm). Achieving high efficiencies with only a few hundred nanometers is a big challenge due to the low capture cross-section for SWIR light (extinction coefficient below 10^4 cm^{-1}). However, an advantage of using thin layers that are in the range of the incident light wavelength is the possibility to create a standing light wave inside the photodiode stack. Reflection and transmission of the light takes place at the interface between two materials due to the difference of their refractive indices. Furthermore, contact metals act as mirrors reflecting all the light back to the photodiode stack. As a result, positive and negative interference takes place, creating points of high and low light intensities. A proper optical design of the devices can shift the highest light intensity to the place where an exciton dissociation center is located, while at the same time minimize losses. This can lead to a significant enhancement of the detector quantum efficiency.

The characteristic optical properties of the materials used, required for the modeling, are incorporated into the complex index of refraction where n is the refractive index and k is the extinction coefficient. Thin layers of QD material are deposited on Si/SiO₂ substrates and measured using variable angle spectroscopic ellipsometry. The data can be fitted using a dispersion law consisting of a Cauchy dependence and Lorentzian absorption peaks for the complex index of refraction. However, due to the low extinction coefficient of the PbS QD films, the ellipsometry data obtained are not sufficient for accurate modeling. In the next phase, values with improved accuracy are

obtained by fitting the transmission and reflection data (R/T) of QD layers on glass. The R/T of three different thicknesses are fitted simultaneously using transfer matrix modeling, starting from the dispersion law as obtained from ellipsometry. Using this approach, the data as shown in **Figure 4** are obtained. The complex index of refraction for the other materials in the photodiode stack is directly obtained from ellipsometry.

The optical constants are subsequently used as an input for a transfer matrix method, adapted to our device structure, simulating the behavior of the light as it impinges on the photodiode.^[34,35] As shown in Figure 4c, the used layers are stacked between a semi-infinite transparent glass substrate and a semi-infinite ambient atmosphere. The light falls into the multilayer from the left, through the glass substrate, and for each layer this can be resolved in two separate terms: a component propagating in the positive (E^+ , moving in the same direction as the incident light) and one in the negative direction (E^-). Using the thickness d_i of each layer and its complex index of refraction \underline{n}_i obtained above, the electrical film of each component can be calculated and subsequently the total electrical field inside our devices can be plotted as below for the wavelength of interest (1440 nm). The expected absorption for the device stack can be retrieved as well as the expected absorption of each individual layer and the expected photodetector EQE at the target wavelength. The developed model comes in full agreement with the experimental data (Figure S4, Supporting Information). Additionally, the thickness of each layer can be optimized to obtain the highest possible EQE values.

First, we simulate the effect of the QD layer thickness on the performance of the device, with fixed thicknesses for the transport layers. In order to incorporate the drift-limited optical active zone in the stack, we split the simulated QD film into two layers: one resembling the depleted layer close to the TiO₂:Nb that will contribute to the photocurrent generation, and one resembling the photocurrent inactive part, in which the generated carriers will recombine. The simulation is performed by sweeping the total QD film thickness and the depletion width. The expected EQE at the wavelength of 1440 nm (**Figure 5a**) demonstrates that for a depletion width in the range of 130 nm, a local maximum of 25% can be reached for a QD film of around 150 nm, while a depletion width larger than 350 nm is required to achieve EQE values above 40%. To check

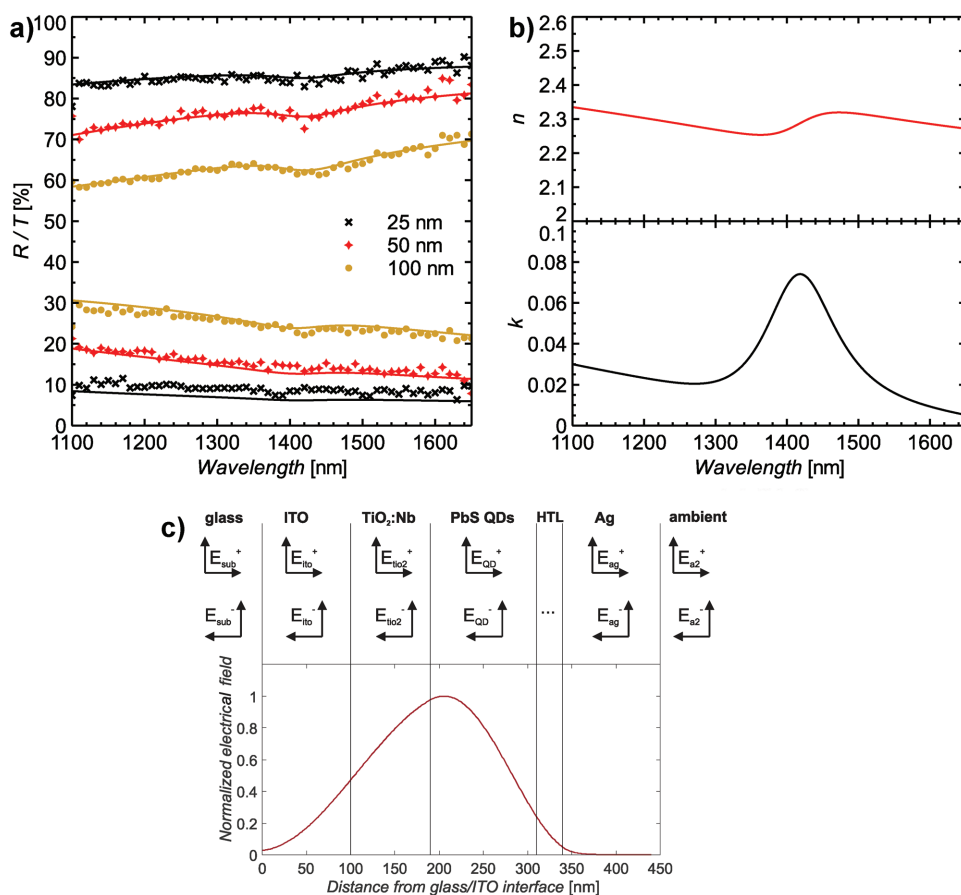


Figure 4. Complex index of refraction measured using variable angle spectroscopic ellipsometry and reflection/transmission measurements. a) Fit of the reflection and transmission data for three different thicknesses of the QD film with the complex index of refraction model determined by ellipsometry. b) The final n and k values for the 5.5 nm QDs demonstrating a peak at about 1440 nm. c) Multiple reflection and transmission in the examined multilayer stack sandwiched between two semi-infinite ambient layers (glass substrate and air). Light is incident from the glass substrate. The electrical field in each layer has two components propagating in the positive (E^+) and the negative (E^-) direction, and together they form the total electrical field. The normalized modulus squared of the electrical field for the wavelength of 1440 nm is plotted.

the validity of the simulations, photodiodes are fabricated with selected QD layer thicknesses in the range of 45–300 nm and transport layer thicknesses at 5 and 20 nm for the HTL and the ETL, respectively. The trend between measured EQE values, the depletion width, and the total QD thickness (Figure 5b) follows

the results predicted by the simulations. Furthermore, the devices with an active layer of 120 ± 10 nm show the highest EQE values; hence, this is the QD layer thickness that can lead to the most efficient photon-to-carrier conversion and should be used for further optimization.

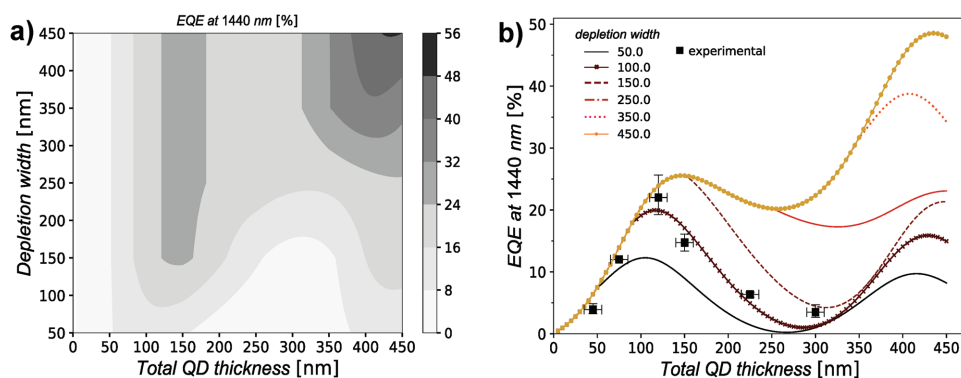


Figure 5. Optical simulations a) monitoring the expected EQE at the wavelength of 1440 nm with variable QD layer thickness and depletion width, and b) comparing the simulated values with the experimental results of fabricated photodiodes. The error bars indicate the uncertainty in the QD layer thickness (± 10 nm) and the variation in the EQE results obtained from measuring different diodes that have the same QD layer thickness.

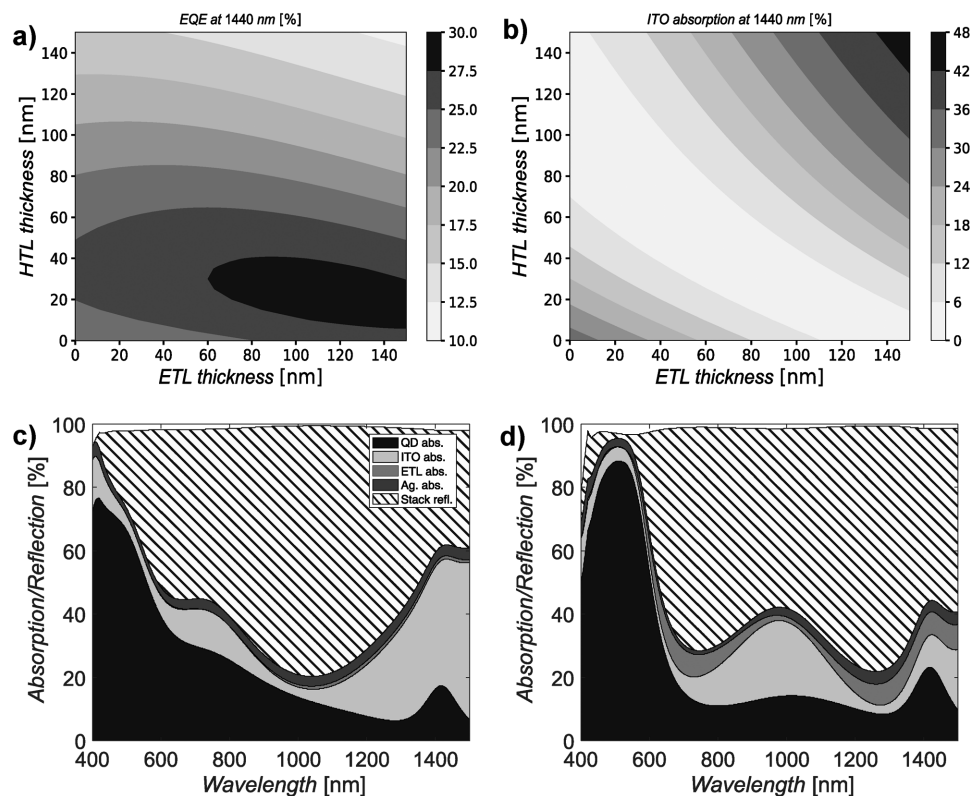


Figure 6. Optimization of carrier harvesting at 1440 nm for a photodiode using a fully depleted 120 nm QD layer and analysis of the optical losses in the full stack. a) Optical simulations for variable transport layer thicknesses in order to achieve the maximum possible EQE, and b) the minimum possible loss in the ITO. c) Before device optimization, the optical loss in the ITO is 40% at 1440 nm, while d) after optimization using 30 and 90 nm of HTL and ETL thickness, respectively, the loss in the ITO is reduced to 10% and the absorption of the QD layer is increased.

Notwithstanding the optimization of the QD layer thickness, further enhancing of the optical cavity can be achieved by fine tuning the other layers in the photodiode stack. By using again optical simulations with a fixed QD layer thickness to the previously found optimum of 120 nm, we analyzed the optical losses in the layer stack used above is shown in **Figure 6**. It is clear that ITO is mainly responsible for these losses, since it is characterized by a high absorption in the IR spectrum, above 40% at the spectral area of 1.4 μm (Figure S4, Supporting Information). To minimize this absorption, simulations are performed by sweeping the $\text{TiO}_2\text{:Nb}$ and the HTL thicknesses and monitoring the expected EQE and ITO absorption (see Figure 6a,b). A proper selection of the transport layer thicknesses will improve the detector EQE notably, while the ITO absorption is minimized. These observed trends are subsequently used as a feedback towards the optimization of the actual devices. The analysis of the optical losses shows indeed a steep decrease in the light lost due to ITO absorption in the target spectrum after the fine tuning of the transport layers. The result is the fabrication of photodiode detectors with enhanced absorption at the wavelength of 1440 nm demonstrating an EQE value higher than 30% as shown in **Figure 7a**. Additionally, these optimized devices are characterized by a dark current lower than $1 \mu\text{A cm}^{-2}$ (Figure 7b) at 2 V reverse bias, leading to a peak in the specific detectivity at the target wavelength with a

value of $\approx 7 \times 10^{11}$ Jones, which is one of the highest reported values for PbS QD photodiode detectors in this range of the IR spectrum.

3. Conclusion

In this work, we describe a methodology for the enhancement of the photogenerated carrier harvesting in PbS QD photodiode detectors for IR light absorption, and use the methodology to optimize a SWIR photodiode. This methodology is based on a combination of thorough analysis of the dominating carrier extraction mechanisms, with optical engineering of the photodiode stack. The aforementioned techniques are applied on photodiodes formed by a heterojunction of a metal oxide ($\text{TiO}_2\text{:Nb}$) and an IR sensitive PbS QD film. Due to the demonstrated short diffusion length, we deduce the need to fabricate fully depleted devices, setting a maximum thickness of 150 nm to the QD layer. For these fully depleted devices, further improvement of the detector performance is realized through an optical design. Using transfer matrix simulations, we maximize the intrinsic cavity effect of the device structure and enhance the EQE of our photodiodes at 1440 nm, reaching values of $\approx 30\%$. Finally, we can conclude that improving the diode junction by increasing the depletion width in the examined system, as well as improving the carrier diffusion length within the QD film, may further improve the quantum efficiency.

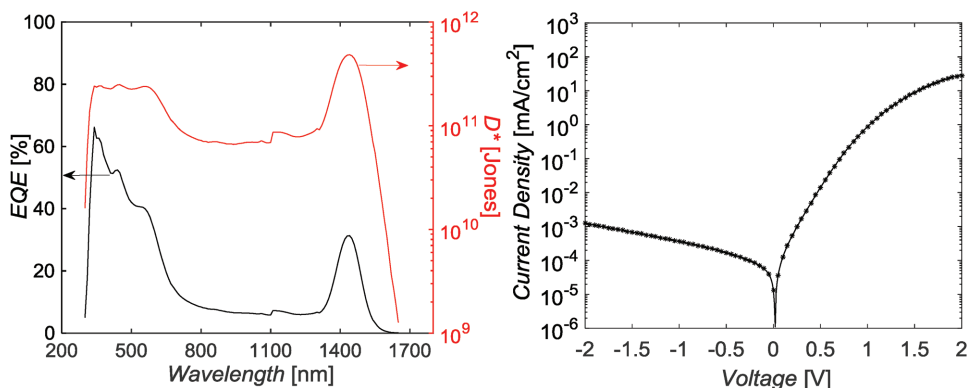


Figure 7. Performance characteristics of the optimized fabricated devices. a) EQE and detectivity. b) Current density under dark conditions.

4. Experimental Section

QD Synthesis: Lead oleate was synthesized from lead trifluoroacetate according to a previously described method.^[21] Also, *N*-4-MeO-phenyl-*N'*-dodecylthiourea was synthesized according to Hendricks et al.^[21] Lead oleate (10.281 g, 13.35 mmol, 1.5 equiv) and *n*-dodecane (150 mL) were added to a 250 mL 3-neck round bottom flask equipped with a stirring bar and coupled to a Schlenk line. The set-up is stirred for 1 h under N_2 flow at 120 °C. In a nitrogen-filled glove box, *N*-4-MeO-phenyl-*N'*-dodecylthiourea (3.0 g, 8.89 mmol) and 1-methoxy-2-(2-methoxyethoxy)ethane (5 mL) were mixed in a 10 mL vial. The vial was sealed with a rubber septum and taken outside. Both vessels were then heated to 135 °C and once the temperature was stable, the solution of thiourea was quickly injected into the clear colorless lead oleate solution via a syringe. The reaction was allowed to run for 5 min at 135 °C before the flask was cooled with a water bath. Once cooled to room temperature, toluene (60 mL) was added and the resulting slurry was split between centrifuge tubes and centrifuged (2000 RCF, 10 min). The dark nanocrystal dispersion was decanted and any remaining solids were discarded. Acetone (150 mL) was then added to precipitate the nanocrystals. After centrifugation (2000 RCF, 5 min), the clear, pale brown solution was discarded and the remaining nanocrystal residue was redispersed in toluene. Five more cycles of precipitation from toluene with acetone were performed to reach a ligand coverage of 4.1 oleate ligands per square nanometer as measured by 1H NMR spectroscopy. Finally, the resulting 1.8 g of 5.5 nm sized PbS QDs were dispersed in *n*-octane and stored in a nitrogen-filled glove box.^[36]

Device Fabrication: The photodiodes were fabricated using a solution-based process except of the top metal contact that was thermally evaporated. $TiO_2:Nb$ dispersion in ethanol^[37] was spin coated on glass substrates with pre-patterned ITO lines cleaned previously in soap, water, acetone, and IPA. Subsequently, the PbS QD film was deposited in air by spin-coating a 15 mg mL⁻¹ solution of PbS QDs in octane. Once dried, 1,4-BDT dissolved in acetonitrile was applied to the substrate for 30 s and spun dry. Then the substrate was washed with acetonitrile. The thickness of the QD film could be increased by repeating the deposition cycles multiple times. Then the poly[*N,N'*-bis(4-butylphenyl)-*N,N'*-bisphenylbenzidine] (polyTPD) was spin coated. The stack was completed with the thermal evaporation of 100 nm of silver (Ag). The device area was defined by the overlap of the top and bottom electrodes at 0.13 cm². For the Schottky diodes, the QD layers were directly deposited on the glass/ITO substrates, while the Schottky junction was formed with the evaporation of 100 nm thick aluminum (Al). For the single carrier devices, poly(3,4-ethylenedioxythiophene)-poly(styrenesulfonate) (PEDOT:PSS; VP AI4083, H. C. Stark) was used as a HTL, spin coated at 2500 rpm from water and annealed at 120 °C for 10 min in order to achieve a 50 nm thick film. Additionally, the 5 nm thick molybdenum oxide (MoO_3) used was thermally evaporated.

CV Measurements: Capacitance–voltage measurements of the diodes were performed using a Keysight E4980A Precision LCR meter, superimposing 10 mV of AC bias over the DC bias and at frequency range between 20 Hz and 1 MHz.

Photoluminescence Measurements: PbS QD films were deposited on quartz substrates using the layer-by-layer technique mentioned above. The PL measurements were performed using a Hamamatsu PL lifetime spectrometer. The QD film was excited by a 532 nm laser and the photoluminescence was measured in wavelengths ranging from 380 up to 1650 nm.

EQE and R/T Measurements: Spectral response measurements were performed using a Bentham PV300 Spectral Response system. A light beam from a Xenon/Quartz halogen source was coupled into a Bentham TMc300 single monochromator, giving a coverage over the spectral range of 300–2500 nm. The reflection and transmission measurements were executed using an integration sphere.

Current–Voltage Characterization: IV sweeps were carried out in N_2 environment using a Keithley 2400 source-meter.

Ellipsometry: Optical constants and film thickness of the materials were measured using a variable angle spectroscopic ellipsometer (Semilab GES5).

Supporting Information

Supporting Information is available from the Wiley Online Library or from the author.

Acknowledgements

The results reported in this work were realized with the funding of Agentschap Innoveren & Ondernemen (VLAIO) in the framework of project MIRIS (IWT/150029).

Conflict of Interest

The authors declare no conflict of interest.

Keywords

carrier transport, infrared light, optical modeling, photodetectors, quantum dots

Received: July 1, 2018
Published online: September 6, 2018

- [1] M. Pilling, P. Gardner, *Chem. Soc. Rev.* **2016**, *45*, 1935.
- [2] J. Jiang, S. Tsao, T. O'Sullivan, M. Razeghi, G. J. Brown, *Infrared Phys. Technol.* **2004**, *45*, 143.
- [3] P. R. Brown, D. Kim, R. R. Lunt, N. Zhao, M. G. Bawendi, J. C. Grossman, V. Bulovic, *ACS Nano* **2014**, *8*, 5863.
- [4] A. Rogalski, *Prog. Quantum Electron.* **2003**, *27*, 59.
- [5] P. E. Malinowski, E. Georgitzikis, J. Maes, I. Vamvaka, F. Frazzica, J. Van Olmen, P. De Moor, P. Heremans, Z. Hens, D. Cheyns, *Sensors* **2017**, *17*, 2867.
- [6] T. Rauch, M. Böberl, S. F. Tedde, J. Fürst, M. V. Kovalenko, G. Hesser, U. Lemmer, W. Heiss, O. Hayden, *Nat. Photonics* **2009**, *3*, 332.
- [7] J. Tang, K. W. Kemp, S. Hoogland, K. S. Jeong, H. Liu, L. Levina, M. Furukawa, X. Wang, R. Debnath, D. Cha, K. W. Chou, A. Fischer, A. Amassian, J. B. Asbury, E. H. Sargent, *Nat. Mater.* **2011**, *10*, 765.
- [8] Z. Zhang, Z. Chen, L. Yuan, W. Chen, J. Yang, B. Wang, X. Wen, J. Zhang, L. Hu, J. A. Stride, G. J. Conibeer, R. J. Patterson, S. Huang, *Adv. Mater.* **2017**, *29*, 1703214.
- [9] X. Lan, O. Voznyy, A. Kiani, F. P. García de Arquer, A. S. Abbas, G.-H. Kim, M. Liu, Z. Yang, G. Walters, J. Xu, M. Yuan, Z. Ning, F. Fan, P. Kanjanaboos, I. Kramer, D. Zhitomirsky, P. Lee, A. Perelgut, S. Hoogland, E. H. Sargent, *Adv. Mater.* **2016**, *28*, 299.
- [10] R. Saran, R. J. Curry, *Nat. Photonics* **2016**, *10*, 81.
- [11] H. Yu, S. Liu, S. Baek, D. Y. Kim, C. Dong, F. So, *J. Mater. Chem. C* **2016**, *4*, 11205.
- [12] I. Moreels, K. Lambert, D. Smeets, D. De Muynck, T. Nollet, J. C. Martins, F. Vanhaecke, A. Vantomme, C. Delerue, G. Allan, Z. Hens, *ACS Nano* **2009**, *3*, 3023.
- [13] Z. Hens, I. Moreels, *J. Mater. Chem.* **2012**, *22*, 10406.
- [14] C. Hu, A. Gassenq, Y. Justo, K. Devloo-Casier, H. Chen, C. Detavernier, Z. Hens, G. Roelkens, *Appl. Phys. Lett.* **2014**, *105*, 171110.
- [15] A. De Iacovo, C. Venettacci, L. Colace, L. Scopa, S. Foglia, *Sci. Rep.* **2016**, *6*, 37913.
- [16] E. Heves, Y. Gurbuz, *Procedia Eng.* **2012**, *47*, 1426.
- [17] E. Heves, C. Ozturk, V. Ozguz, Y. Gurbuz, *IEEE Electron Device Lett.* **2013**, *34*, 662.
- [18] J. P. Clifford, G. Konstantatos, K. W. Johnston, S. Hoogland, L. Levina, E. H. Sargent, *Nat. Nanotechnol.* **2009**, *4*, 40.
- [19] M. Yuan, M. Liu, E. H. Sargent, *Nat. Energy* **2016**, *1*, 16016.
- [20] B. N. Pal, I. Robel, A. Mohite, R. Laocharoensuk, D. J. Werder, V. I. Klimov, *Adv. Funct. Mater.* **2012**, *22*, 1741.
- [21] M. P. Hendricks, M. P. Campos, G. T. Cleveland, I. Jen-La Plante, J. S. Owen, *Science* **2015**, *348*, 1226.
- [22] A. Hadipour, Imec Vzw, WO2017108710A1, **2017**.
- [23] D.-K. Ko, A. Maurano, S. K. Suh, D. Kim, G. W. Hwang, J. C. Grossman, V. Bulović, M. G. Bawendi, *ACS Nano* **2016**, *10*, 3382.
- [24] J. Tang, L. Brzozowski, D. A. R. Barkhouse, X. Wang, R. Debnath, R. Wolowicz, E. Palmiano, L. Levina, A. G. Pattantyus-Abraham, D. Jamakosmanovic, E. H. Sargent, *ACS Nano* **2010**, *4*, 869.
- [25] T. Salim, Z. Yin, S. Sun, X. Huang, H. Zhang, Y. M. Lam, *ACS Appl. Mater. Interfaces* **2011**, *3*, 1063.
- [26] A. Trenczek-Zajac, M. Rekas, *Mater. Sci.* **2006**, *24*, 53.
- [27] H. Wu, L. Wang, *J. Chem. Phys.* **1997**, *107*, 8221.
- [28] J. Wang, J. Polleux, J. Lim, B. Dunn, *J. Phys. Chem. C* **2007**, *111*, 14925.
- [29] B. R. Hyun, Y. W. Zhong, A. C. Bartnik, L. F. Sun, H. D. Abruna, F. W. Wise, J. D. Goodreau, J. R. Matthews, T. M. Leslie, N. F. Borrelli, *ACS Nano* **2008**, *2*, 2206.
- [30] S. M. Sze, K. K. Ng, *Phys. Semicond. Devices*, 3rd ed. John Wiley Sons, Inc., Hoboken, NJ **2007**, p. 164.
- [31] D. D. W. Grinolds, P. R. Brown, D. K. Harris, V. Bulovic, M. G. Bawendi, *Nano Lett.* **2015**, *15*, 21.
- [32] J. H. Warner, E. Thomsen, A. R. Watt, N. R. Heckenberg, H. Rubinsztein-Dunlop, *Nanotechnology* **2005**, *16*, 175.
- [33] J. Kwan Kim, J. H. Song, H. Choi, S. Jae Baik, S. Jeong, *J. Appl. Phys.* **2014**, *115*, 054302.
- [34] L. A. A. Pettersson, L. S. Roman, O. Inganäs, *J. Appl. Phys.* **1999**, *86*, 487.
- [35] H. Gommans, D. Cheyns, T. Aernouts, C. Girotto, J. Poortmans, P. Heremans, *Adv. Funct. Mater.* **2007**, *17*, 2653.
- [36] J. Maes, N. Castro, K. De Nolf, W. Walravens, B. Abécassis, Z. Hens, *Chem. Mater.* **2018**, *30*, 3952.
- [37] M. Niederberger, *Acc. Chem. Res.* **2007**, *40*, 793.